Single Molecule Quantum-Confined Stark Effect Measurements of Semiconductor Nanoparticles at Room Temperature

KyoungWon Park,[†] Zvicka Deutsch,[‡] J. Jack Li,[§] Dan Oron,[‡] and Shimon Weiss[§,⊥,∥,*]

[†]Electrical Engineering Department, Henry Samueli School of Engineering and Applied Science, University of California, Los Angeles, California 90095, United States, [‡]Department of Physics, The Weizmann Institute, Rehovot 76100, Israel, and [§]Department of Chemistry & Biochemistry, [⊥]Department of Physiology, and [∥]California NanoSystems Institute, University of California, Los Angeles, California 90095, United States

ABSTRACT We measured the quantum-confined Stark effect (QCSE) of several types of fluorescent colloidal semiconductor quantum dots and nanorods at the single molecule level at room temperature. These measurements demonstrate the possible utility of these nanoparticles for local electric field (voltage) sensing on the nanoscale. Here we show that charge separation across one (or more) heterostructure interface(s) with type-II band alignment (and the associated induced dipole) is crucial for an enhanced QCSE. To further gain insight into the experimental results, we numerically solved the Schrödinger and Poisson equations under self-consistent field approximation, including dielectric inhomogeneities. Both calculations and experiments suggest that the degree of initial charge separation (and the associated exciton binding energy) determines the magnitude of the QCSE in these structures.

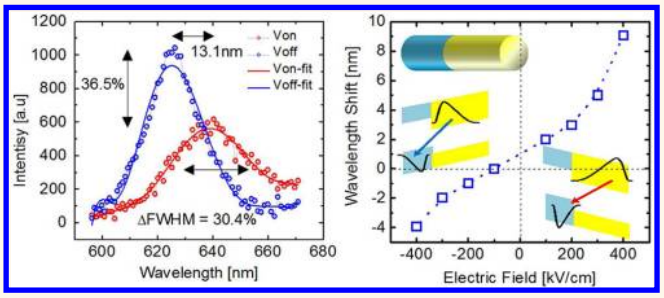

KEYWORDS: quantum dot · nanorod · type-I band alignment · type-II band alignment · quantum-confined Stark effect · voltage sensing · wave function engineering

Colloidal semiconductor quantum dots (QDs) and nanorods (NRs) are nanometer-sized single-crystal nanoparticles (NPs) nucleated from a hot solution of precursor molecules. Their size and shape can be precisely controlled by the duration, temperature, and ligands used in the synthesis.[1−3] This method yields QDs or NRs that have composition and size-dependent absorption and emission wavelengths covering the entire spectral range from the visible to the NIR regions.[4] In addition to fluorescence, QDs and NRs possess other interesting optoelectronic, electrochemical, and magnetic properties that are likely to be further exploited. Such NPs have found numerous applications, such as in biological tagging,[5] quantum optics,[6] photovoltaic light harvesting,[7] flat panel displays,[8] and others.

The growing number of novel applications stems from the ever-increasing control over QDs' and NRs' optical and electronic properties, afforded by dramatic improvements in synthetic protocols. Significant advancements include shape control *via* addition of co-adsorbents,[9] allowing the fabrication of quantum rods and tetrapods and synthesis of core/shell nanocrystals with type-I and type-II band alignments.[10] Combination of these synthetic techniques has afforded the fabrication of asymmetric heterostructures *via* seeded nanorod formation[11,12] where a CdSe or a ZnSe core is embedded in one end of a CdS rod, exhibiting strongly asymmetric localization regimes for the electrons and the holes. Type-II QDs have been shown to have controllable exciton−exciton interaction energies,[13] which is of particular interest for optical gain[14] and light-harvesting[7] applications. Nucleation doping, a recent addition to the synthesis toolbox, enables formation of shallow traps for one charge carrier within the QD or NR, affording a controlled separation of charges inside the nanoparticle.[15]

* Address correspondence to sweiss@chem.ucla.edu.

Received for review August 15, 2012 and accepted October 17, 2012.

Published online 10.1021/nn303719m

The intricate control over size, shape, shell thickness, doping, heterostructure, and band alignment allows precise engineering of the carriers' wave functions and, in particular, their interactions with (and perturbation by) the immediate local environment. As a result, QDs and NRs have been increasingly used as local probes of their nanoscale environment. Examples include sensing of chemical properties such as pH,[16] anion,[17] and ion detection[18] and physical properties such as light intensity,[19] temperature,[20] stress,[21] and surface charge.[22]

The utilization of QDs and NRs for local electric field (F) sensing is one such additional interesting proposition. It is well-established that semiconductor absorption and emission edges are modulated by an external electric field and even more so when optically excited electron–hole pairs (and excitons) are confined in small dimensions (as compared to the exciton's Bohr radius), giving rise to the quantum-confined Stark effect (QCSE).[23] The physical origin of this effect is in the separation of the photoexcited charges, creating a dipole that opposes the external electric field. QCSE was first demonstrated for two-dimensional (epitaxially grown) layers of quantum wells and was used to construct devices such as the self-electro-optic effect device (SEED).[24] QCSE-based SEED has advantages such as low power consumption, high speed, easy integration onto a Si-based device or waveguide, and room temperature (RT) operation.[25]

QCSE in epitaxially grown 2D quantum wells is more readily observed as compared to the effect in colloidal NPs. This is because the induced internal field is larger when the dielectric constant (ε_r) of the potential well is similar to the dielectric constant of its surroundings. For example, a wavelength shift of 15 nm was measured (shift from 610 nm at 5 V to 625 nm at 10 V) at 197 K ($\Delta\lambda/\lambda = 2.40\%$ for $\Delta F = 119$ kV/cm).[26] For type-II band alignment, even larger changes were measured ($\Delta\lambda$ = 85 nm, $\Delta\lambda/\lambda$ = 7.14% for ΔF = 80 kV/cm).[27] Nonetheless, the advent of colloidal QD synthesis led to extensive examination, mostly at low temperature (LT), of their QCSE.[28] Wavelength shifts of type-I NPs are usually small ($\Delta\lambda$ = 6.0 nm, $\Delta\lambda/\lambda$ = 1.0% for ΔF = 350 kV/cm).[29] Larger shifts were measured for type-II NRs ($\Delta\lambda$ = 4.2 nm, $\Delta\lambda/\lambda$ = 0.65% for ΔF = 30 kV/cm).[30]

Due to thermal excitations, the exciton is readily ionized at RT, making it more difficult to observe the Stark effect in these particles. Moreover, trapping of random thermally excited charges at surface and interface states can cause local potential fluctuations that interfere with and modulate charge separation, diminishing the effect. Nonetheless, when compared to voltage-sensitive organic dyes, QCSE has the potential to replace a (noisy) intensity change (ΔI) measurement with a (less noisy) ratiometric measurement.

The question we set up to answer in this study is: could NPs be engineered to yield a sizable QCSE at RT? Moreover, could the effect be measured, with a relatively short integration time, on a single particle? Could we expect high enough sensitivity ($\Delta\lambda/\lambda$) in hydrated environment (ε_r = 80) as compared to conventional voltage-sensitive dyes (which exhibit up to $\Delta I/I \sim 20\%$ for ΔV = 100 mV)?[31] Affirmative answers to these questions could imply that such NPs could act as local voltage sensors on the nanoscale (displaying changes in fluorescence quantum yield, fluorescence lifetime, and/or peak emission wavelength in response to the local electric field).

RESULTS AND DISCUSSION

Description of NPs Tested in This Study. Eight NPs of different geometries, band alignment structures, and compositions were surveyed for their QCSE (Table 1). Samples were of either type-I or type-II band alignment, homostructures, or heterostructures and of either sphere or rod shapes. Table 1 describes the attributes of these samples and includes their transmission electron microscopy (TEM) micrographs. Average sizes of the various samples were evaluated from TEM images (from 30 NPs or more each) and are summarized in Table S1 in the Supporting Information. Samples #1 and #2 are homogeneous CdSe NRs with different lengths (7.7 and 43.4 nm on average, respectively). Samples #3 and #4 are quasi-type-II CdS NR heterostructures with CdSe QDs as seed with different rod lengths (12.8 and 29.0 nm, respectively), where electrons are delocalized across the entire NR while the holes are localized on CdSe seed. Samples #5 and #6 are CdTe/CdSe core/shell type-II QDs having different core sizes and shell thicknesses. Sample #5 has a 4.2 nm CdTe core and a two-layer CdSe shell, and sample #6 has a 3.9 nm CdTe core and a five-layer CdSe shell. Sample #7 is an asymmetric type-II heterostructure composed of a ZnSe sphere embedded in a thick bullet-shaped CdS NR (seeded NR). Its length is 33.7 nm, and width at the thicker waist is 12.1 nm. We note that sample #8 is a novel formulation with a barrier inserted inside a type-II gap and was only recently described in the context of quantum optics application.[32] Particles are hammer-shaped, 28.0 nm long, and 5.0 nm wide at the "handle". Excitons in this sample have two recombination pathways, one from the conduction band of CdSe to the Te dopant level (spatially direct gap, 730 nm transition) and the other from the conduction band of CdSe to the valence band of CdZnSe (spatially indirect gap, 630 nm transition). The 730 nm emission is due to a type-I transition, while the 630 nm emission is the manifestation of an enhanced type-II transition since the electron and the hole reside in two wells that are separated by a CdS barrier. The emission spectrum of this sample is shown in Figure S12. Interestingly, the spectral bandwidth of

TABLE 1. List of Studied Samples and Their Relevant Attributes[a]

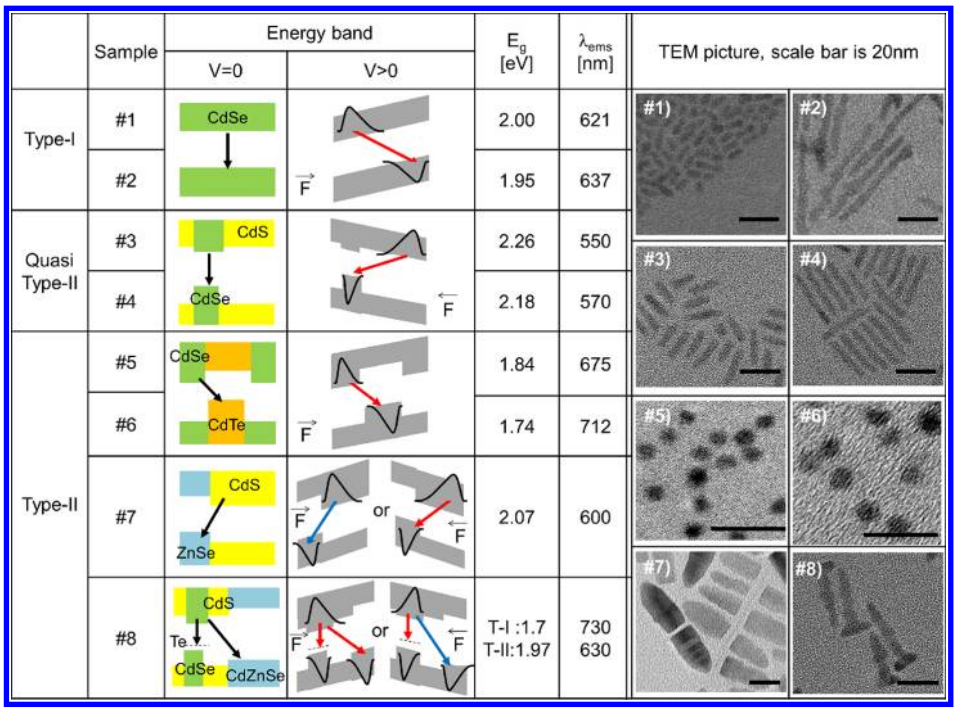

[a] E_g and λ_{ems} are the respective NP's optical band gap and peak emission wavelength. Black arrow represents a radiative recombination pathway without electric field (F). When F is applied, λ_{ems} is either increased (red arrow) or decreased (blue arrow) depending on the NPs' composition and its relative orientation with respect to the direction of F. Transmission electron microscopy (TEM) micrographs of all samples are shown on the right panel.

the type-II transition is much narrower than the spectral bandwidth of the type-I transition. Unlike previously observed line width differences in two color emitting CdSe/ZnS/CdSe core/barrier/shell systems,[33] this is probably due to stronger phonon coupling of the type-I transition due to the strong hole localization in the doped core.[32] Both samples #7 and #8 are asymmetric type-II NPs. As discussed below, and elsewhere,[34,35] the spectral shift dependences on the applied field are expected to be different for these samples as compared to type-I, quasi-type-II, and symmetric type-II QDs and NRs (samples #1−#6).

QCSE Results for Type-I and Quasi-Type-II NPs (Samples #1−#4). RT QCSE results for CdSe NRs (sample #2) are shown in Figure 1. The figure shows 200 successive spectra of a single NR. As clearly shown in Figure 1a,b, the seeded NR exhibited fluorescent intermittency (blinking)[36−39] with a typical blinking-on/blinking-off telegraph noise-like intensity values. Only frames during blinking-on periods were retained for further analysis using a threshold filter (Figure 1b and SI-5 in Supporting Information).

Figure 1c shows sample #2's average spectra (over the whole movie) for V_{off} and V_{on}, where the latter is red-shifted with respect to the former by 2.0 nm, corresponding to $\Delta\lambda/\lambda$ = 0.32%. Concomitant with the spectral shift, a 16.4% decrease in the peak emission intensity and a 13% increase in the fwhm of the emission peak were observed (Figure 1c) based on the fitted curves. Beyond averaging these properties over the whole movie (20 s, Figure 1c), we also analyzed the spectral shifts for individual frames (0.1 s each, Figure 1d), by extracting emission peak wavelength (λ_{peak}) for each frame (in the blinking-on state) and separately histogramming the V_{off} and V_{on} frames (Figure 1d). This analysis yields λ = 635.9 ± 0.5 and 638.4 ± 1.4 nm for V_{off} and V_{on}, respectively, with a red shift $\Delta\lambda$ = 2.5 nm (as compared to $\Delta\lambda$ = 2.0 nm in Figure 1c). The difference between Figure 1c,d is originated from the fitting errors and their accumulation. Figure 1e shows the difference between the two spectra in Figure 1c.

The averaged V_{off} and V_{on} spectra (Figure 1c), the histograms of V_{off} and V_{on} peak wavelength (Figure 1d), and the shape of the differential spectra (Figure 1e) clearly demonstrate spectral red shift and spectral broadening due to the applied external field, which are hallmarks of the QCSE and a manifestation of the exciton's charge separation, reflecting the buildup of an internal electric field (dipole) that opposes the external applied field.

A more pronounced QCSE was measured for sample #4 (Figure 2), with noticeable spectral and integrated intensity changes (Figures 2a,b; notice the sawtooth signal in Figure 2b). The average spectral shift $\Delta\lambda$ was measured to be 4.4 nm ($\Delta\lambda/\lambda$ = 0.77%).

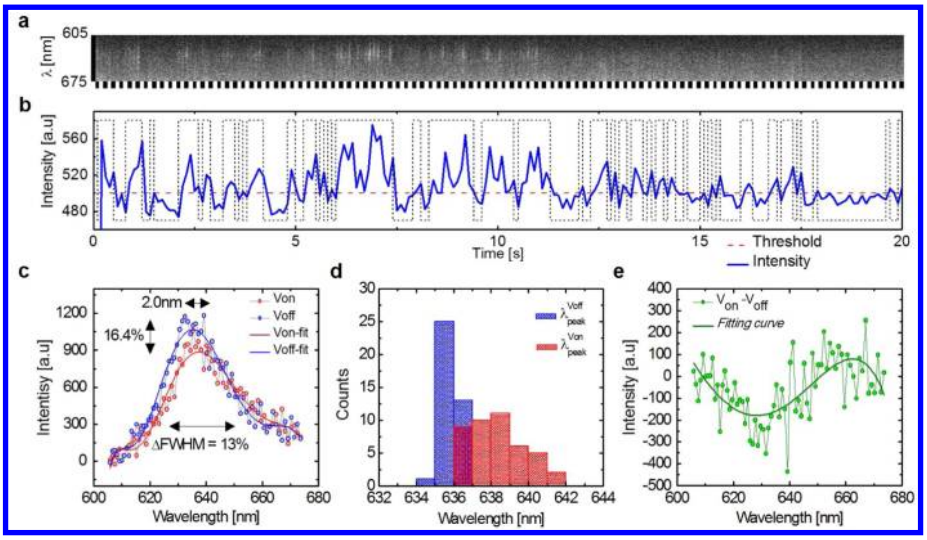

Figure 1. Single NP QCSE analysis of sample #2. (a) Series of 200 successive spectra obtained from sample #2 at RT (excitation intensity 2 mW/cm^2, electric field modulation frequency 10 Hz, single frame integration of 0.1 s). The dashed white/black line at the bottom of the figure indicates the periods at which the applied electric field was on (V_{on} = 400 kV/cm, white) or off (V_{off} = 0 kV/cm, black). (b) Integrated intensity trajectory (integration over λ for each frame) of the data shown in a (solid blue). The dashed red line is a guide to the eye emphasizing the blinking-on and blinking-off intensity states. (c) Averaged V_{on} frames (red) and averaged V_{off} frames (blue) (after filtering for frames in the blinking-on state) with corresponding seventh order polynomial fits (solid red and blue, respectively). (d) Histogram of spectral peak positions (V_{on} red, V_{off} blue) from all blinking-on frames (derived from the polynomial fits). (e) Differential emission spectra derived from c (see SI-5).

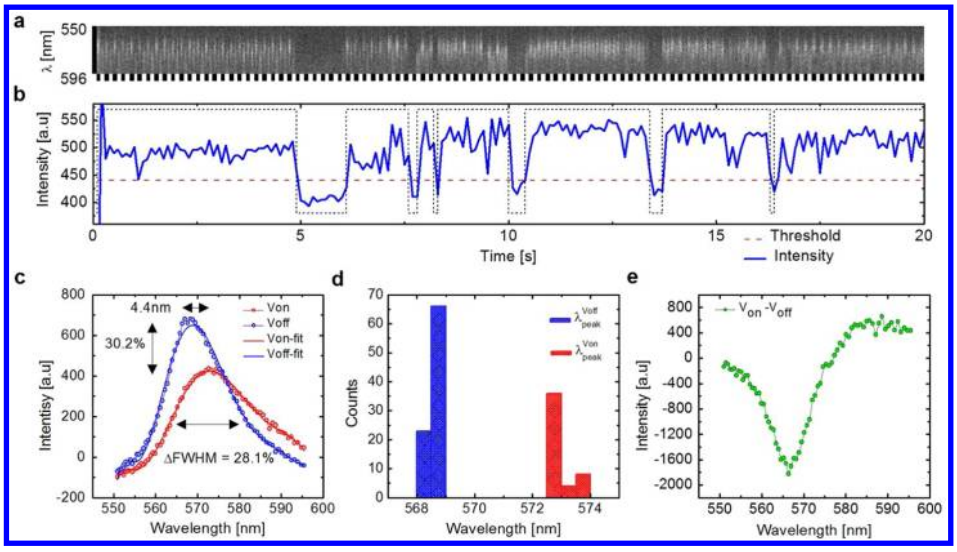

Figure 2. Single NP's QCSE analysis of sample #4, presented in the same format as in Figure 1.

A 30.2% decrease in peak intensity and 28.1% increase in fwhm were observed (Figure 2c). These numbers represent a QCSE which is about twice as big for sample #4 as compared to sample #2. The peak spectra (λ_{peaks}) histograms for V_{off} and V_{on} are λ = 568.7 $\pm$ 0.3 and 573.9 $\pm$ 1.2 nm, respectively, and are clearly separated (Figure 2d), displaying a red shift of $\Delta\lambda$ = 5.23 nm (as compared to $\Delta\lambda$ = 4.4 nm in Figure 2c). However, majority of sample #4 NPs displayed smaller shifts.

It is apparent from the spread (and the overlap) of the V_{off} and V_{on} histograms that the magnitude of the Stark effect varies from NR to NR, likely due to several reasons: (i) the orientation of NRs with respect to the applied field (due to only partial alignment); (ii) inhomogeneities in NRs' structure and size; (iii) presence of defects and/or traps on NRs surfaces and interfaces; (iv) presence of random surface charges on the supporting slide in close proximity to the NRs and others. Charge trapping due to (iii) or (iv) could stochastically (and temporally) modulate the QCSE and result in static or dynamic broadening (spectral diffusion). The fast ionization of the exciton at RT, the observed inhomogeneities, and the activation of trap states reduce the observed effect at RT as compared to low temperature (LT). Nonetheless, Figures 1 and 2 show that, although

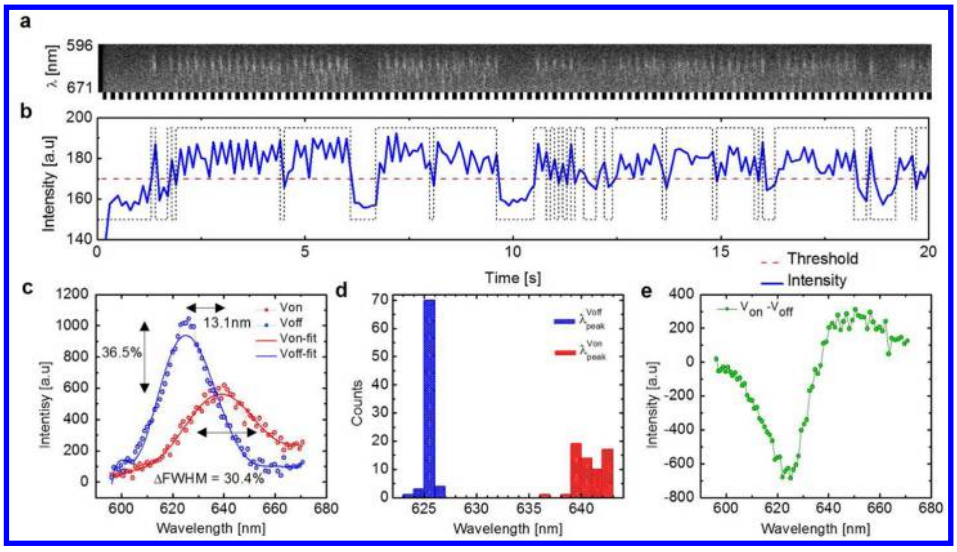

Figure 3. Single NP's QCSE analysis of sample #8, presented in the same format as in Figure 1.

the effect is very small for these samples, it still can be measured at RT, on the single particle level, and therefore, it should be possible to screen a library of different NPs for the optimal structure, shape, size, composition, and band alignment in order to yield a larger QCSE at RT.

The experiments described in Figures 1 and 2 were repeated tens of times for each of the samples in Table 1 such that statistically meaningful QCSE data could be histogrammed from many individual NPs. Figure S10 shows histograms for samples #1−#4. Samples were subjected to the alignment procedure during deposition on the coverslip (SI-3) except for the data described in Figure S10e (serving as a control for alignment).

Samples #1 and #2 are homogeneous NRs with different diameter × length dimensions: 2.9 × 7.7 nm and 4.2 × 43.4 nm, respectively. If electron and hole separation is extended throughout the length of the NR, sample #2 should yield a larger shift than sample #1. We observe, however, similar average shifts ($\Delta\lambda$ = 0.6 ± 1.2 nm, $\Delta\lambda$ = 0.6 ± 1.4 nm) for both samples, suggesting incomplete charge separation along the long axis of the NRs.

NPs with the structure, shape, and materials' compositions of samples #3 and #4 (CdSe/CdS seeded rods) were previously reported to have (i) a high photoluminescent quantum yield (QY) (75% at RT[40]); (ii) a high degree of emission polarization;[40] (iii) an aspect ratio (or length) dependent QCSE[41] at LT; and (iv) an efficient charge separation at RT.[42] These attributes make these NPs ideal for studying length- and orientation-dependent QCSE. However, in contrast to the reported LT results, we could not detect statistically significant differences in Stark effects for aligned ($\Delta\lambda$ = 0.7 ± 1.4 nm) and nonaligned ($\Delta\lambda$ = 0.6 ± 1.2 nm) samples (Figure S10d,e), although polarization measurements suggested otherwise (SI-3). We could not detect statistically significant differences in wavelength shifts for the two different lengths and aspect ratios either (average shifts were around ~0.7 nm with 4.0 nm outliers, Figure S10c,d). A possible explanation for this observation is mis-classification of the CdSe/CdS interface as a quasi-type-II. The conduction band offset (Δe) of CdSe/CdS could vary in the range 0.00 to 0.30 eV[43] (depending on geometry and strain), while the valence band offset (Δh) is estimated to be 0.78 eV. If core diameters are larger than 2.8 nm, it could possibly still be confined to the CdSe seed, therefore reducing the extent of charge separation.

We note that all histograms in Figure S10 have tails with negative values (representing QCSE blue shifts), consisting of approximately 15% of all measured NPs. These are likely due to built-in dipole moments induced by random surface charge configurations that cancel out the external field and generate a residual field in the opposite direction.[28] Shifts from such random charges are estimated to contribute "noise" of about ±2 nm to the QCSE measurements. We conclude that the extent of charge separation at RT in samples #1−#4 (homogeneous and quasi-type-II structures) is small and does not (or very weakly) depend on NR's length or orientation.

QCSE Results for Type-II NPs (Samples #5−#8). Similar QCSE measurements were performed for samples #5−#8, all having type-II band alignment (Table 1). Figure 3 shows representative results for a single NP from sample #8. A clear zigzag pattern of alternating V_{off} and V_{on} spectra is observed in the raw data of Figure 3a (most notably around 6 and 9 s). This zigzag pattern is also manifested in the integrated intensity trajectory during the blinking-on periods (Figure 3b), a manifestation of the decreased intensity in the V_{on} state (Figure 3c). Figure 3c shows the averaged V_{on} frames (red) and averaged V_{off} frames (blue) for the

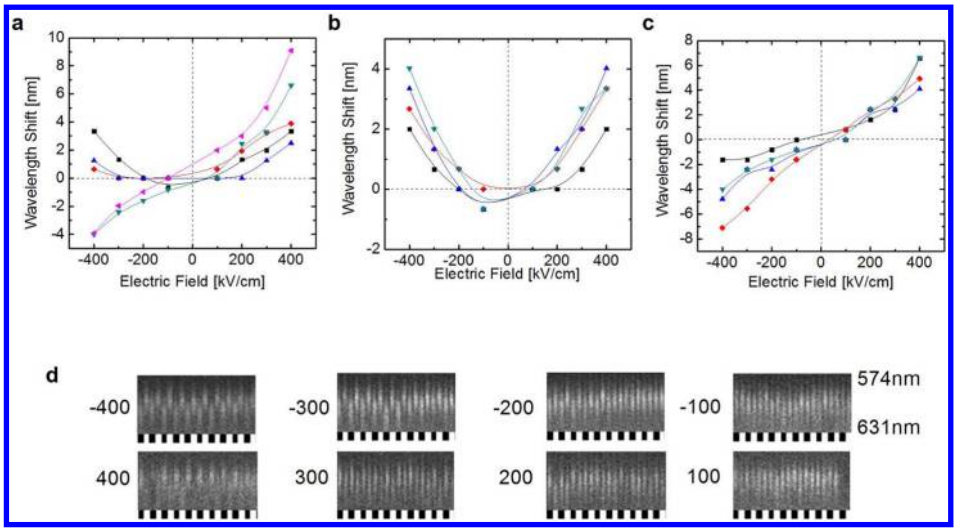

Figure 4. Field-dependent QCSE of single NP. (a) Samples #2 (black squares), #4 (red diamonds), #6 (blue triangles), #7 (dark cyan down triangles), #8 (pink left triangles). (b,c) Four individual NP of sample #2 (b) and sample #7 (c). (d) Spectral images for 20 frames of sample #7 (presented as red diamonds in c). Applied electric field (kV/cm) is shown at the left of each image, and λ is shown at the right side of the image of −100 kV/cm field.

whole trajectory, exhibiting an average $\Delta\lambda$ = 13.1 nm ($\Delta\lambda/\lambda$ = 2.1%) wavelength shift, 36.5% peak intensity (ΔI) reduction, and 30.4% fwhm (Δfwhm) increase, which are, respectively, 6.6×, 2.2×, and 2.3× larger than the corresponding changes presented in Figure 1c for sample #2. In contrast to Figure 1d, the V_{off} and V_{on} spectral peak position histograms (Figure 3d) are well separated, suggesting the QCSE could be detected with high confidence in a single frame (0.1 s) for a single NP, while 20 s averaging was needed to extract the shift in Figure 1. The large shift is also evident from the differential spectrum (Figure 3e, as compared to the noisy differential spectrum of Figure 1e).

Statistically meaningful data were also acquired for samples #5−#8. While similar wavelength shifts were observed for samples #1−#4 (Figure S10), large variations were observed among type-II NPs (samples #5−#8, Figure S11). Samples #5 and #6 are spherical CdTe/CdSe (core/shell) type-II QDs with core diameters at around 4 nm and shell thicknesses of around 1−2 nm. They have smaller QCSE than type-I NRs (average $\Delta\lambda$ =0.5 ± 1.2 and 0.4 ± 1.3 nm for samples #5 and #6, respectively, and $\Delta\lambda$ = 3.1 nm maximum shifts for both, Figure S11a,b). Sample #7 is a bullet-shape type-II ZnSe (sphere) seeded CdS NR, and it displays both red and blue spectral shifts due to its asymmetry. Wavelength blue shift in QCSE is a unique feature of asymmetric type-II quantum structures and was previously measured only for 2D quantum well devices.[34,35,44] Type-II band alignment assists in charge separation; the symmetry breaking of a single heterostructure implies that the electric field either pushes both the electron and the hole wave functions toward the interface, leading to a blue shift, or away from the interface (further enhancing charge separation) leading to a red shift. However, blue shifts do not occur in symmetric core−shell structures such as samples #5 and #6. Sample #7, in contrast, has an asymmetric type-II interface, allowing for charges to be pushed toward the interface or away from it, depending on the direction of the applied electric field.

The measured blue shifts as well as red shifts for sample #7 are favorably compared with red shifts reported for samples #1−#6, with a $\Delta\lambda$ = 1.6 ± 1.7 nm average shift and up to $\Delta\lambda$ = 8.2 nm for outliers (Figure S11c). Even larger shifts (as large as $\Delta\lambda$ = 13.1 nm, Figure 3) were observed for the type-II transition of sample #8 (this sample has ∼730 nm type-I transition and ∼630 nm type-II transition due to an asymmetric type-II interface), with an average shift of $\Delta\lambda$ = 3.5 ± 3.1 nm (Figure S11e). The type-I transition of sample #8 displayed an average shift of $\Delta\lambda$ = 1.2 ± 2.0 nm and up to $\Delta\lambda$ = 6.5 nm for outliers (Figure S11d).

Field Dependence of the QCSE. All QCSE data presented so far (Figures 1−3 and Figures S10 and S11) were measured at a fixed (maximal) V_{on} electric field (400 kV/cm). We also measured the field dependence of the QCSE ($\Delta\lambda$-F) for samples #2, #4, #6, #7 and #8 (samples #1, #3 and #5 displayed too small QCSE). The electric field was varied from −400 kV/cm to +400 kV/cm in 100 kV/cm increments. Figure 4a displays $\Delta\lambda$-F plots for the different samples. For example, sample #2 showed a quadratic $\Delta\lambda-F$ relationship as previously reported elsewhere,[28,29] while sample #4 showed an asymmetric $\Delta\lambda-F$ as reported by Müller *et al.*[41] Due to its symmetrical core−shell type-II structure, sample #6 also displayed a quadratic relation (similar to the type-I sample #2). However, sample #7 and the type-II transition of sample #8 displayed roughly linear $\Delta\lambda-F$ due to symmetry breaking (*i.e.*, the relative orientation of the applied field with respect to the type-II asymmetry of the structure). We note that the linear $\Delta\lambda-F$

was observed for multiple quantum wells (MQWs) or superlattices,[44] but both red and blue shifts were simultaneously present in the spectrum (and therefore required spectral demixing for the analysis). Linear $\Delta\lambda - F$ relation is well-resolved here, manifesting the presence of a single asymmetric type-II interface (at very high fields, this relation could be altered[35]). Figure 4b,c displays $\Delta\lambda - F$ curves for four different sample #2 NPs (middle) and 4 different sample #7 NPs (right). These curves represent the reproducibility of the QCSE among individual NPs from the same sample and the robust and clear distinction in QCSE between type-I and asymmetric type-II structures. Figure 4d shows 2 s stretches (20 frames) of field-dependent spectral shift raw data of a single NR from sample #7 (corresponding to red diamonds in Figure 4c).

Simulations Results. The experimental results suggest a smaller extent of charge separation in type-I and quasi-type-II NRs as compared to asymmetric type-II structures. In order to gain deeper insight and understanding for why this is so, we performed QCSE simulations for all samples shown in Figure 4a. We solved the self-consistent Schrödinger−Poisson equations numerically (see SI-6). The simulations are in good agreement with previously published calculations[28,29,45,46] and the experiments presented here. Dimensions and parameters used for these simulations are presented in SI-7. Table 2 compares the experimentally obtained maximum red (or blue) shifts with the corresponding simulated shifts and excitons' binding energies (E_b). Except for sample #6, simulations agree well with experiments. It is possible that our geometrical definition and parameters for sample #6, as given in SI-7, are not as good as for other samples. For example, CdTe/CdSe core/shell structures are easily branched into shapes such as tetrapod. It is possible that our samples exhibit initial small branching not detected by TEM (due to sample's aging or residual tetradecylphosphonic acid ligands that are not easily removed during TEM sample preparation). We also extracted the overlap integral $\langle\psi_e|\psi_h\rangle^2$ (Figure 5a) as a measure of charge separation. The overlap integral has a maximal value at zero field for the type-I NP (sample #2) and for the symmetric core−shell type-II QD (sample #6). This is also reflected in the quadratic $\Delta\lambda - F$ relation for these samples. However, the overlap reaches its maximal value at the negative maximal field (−400 kV/cm) for asymmetric heterostructures (type-II samples #7 and #8 and quasi-type-II sample #4) in which both the electron and the hole are pushed toward each other and against the heterostructure interface (see corresponding band diagrams in Table 1). This is also reflected in the nearly linear $\Delta\lambda - F$ relation for these samples. Similarly to the experimental results, simulations show that the charge separation in sample #2 turns out to be small (8% reduction in overlap integral) due to the strong exciton's binding energy (E_b = 40.04 meV). Simulations for sample #4 show a sudden drop (17%) in the overlap integral at around 300 to 400 kV/cm, likely due to exciton ionization. The overlap integral for sample #6 does not exhibit a change as a function of applied field due to the small size of the particle (charge separation is limited by the physical dimensions). Samples #7 and #8 exhibit minimal overlap since the exciton's binding energy is negligible (E_b = 3.34 and 0.03 meV, respectively) and so is the Coulomb interaction for these samples. Figure 5b compares field-dependent $\Delta\lambda$ values of calculation and experimental data of samples #2 and #8 (same

TABLE 2. Experimental and Calculated Maximum $\Delta\lambda$ (at 400 kV/cm) and E_b; $\Delta\lambda$ Blue Shifts (at −400 kV/cm) Are Shown in Parentheses

sample	exptl $\Delta\lambda$ (nm)	calcd $\Delta\lambda$ (nm)	E_b (meV)
#2	4.0	3.1	40.04
#4	4.4	4.8	50.22
#6	3.1	1.5	21.94
#7	8.2 (−7.1)	12.4 (−7.6)	3.34
#8	13.1 (−7.3)	15.5 (−10.2)	0.03

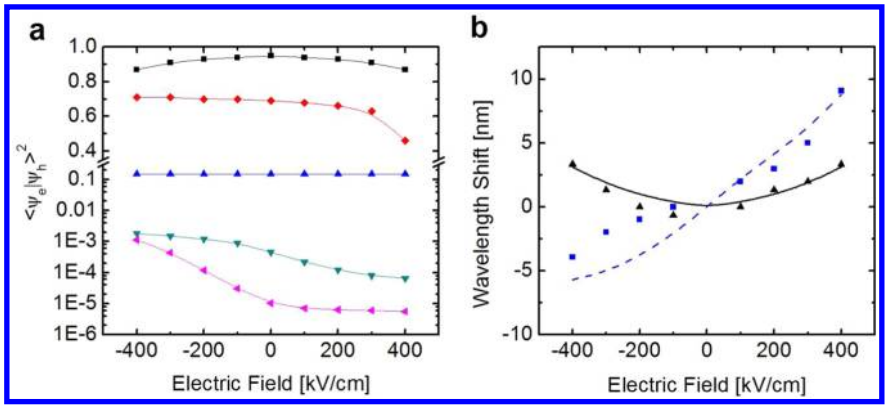

Figure 5. Calculation results. (a) Overlap integral of samples #2 (black squares), #4 (red diamonds), #6 (blue triangles), #7 (dark cyan down triangles), and #8 (pink left triangles). The *y*-axis has a log scale for 1×10^{-6}−0.3 and a linear scale for 0.35−1.0. (b) Field dependence ($\Delta\lambda - F$) of experiment (black triangles and blue squares) and simulation (solid and dashed line) of samples #2 (black) and #8 (blue), respectively.

data as in Figure 4a). Calculated $\Delta\lambda$ of sample #2 regenerates the experiment data. For sample #8, we assume partial alignment with an angle θ between the NR's long axis and the field direction and a maximal possible shift of 13.1 nm at $\theta = 0$. The data could then be reasonably fitted with a $\cos^2\theta$ ($\theta \approx 37°$) correction factor (Figure 5b).

DISCUSSION

Most of previous single NP Stark effect measurements were performed at cryogenic temperatures.[28,29,41] The few RT[30,42] studies were done on the ensemble level with NPs embedded in polymer matrixes or in solvents with large dielectric constants ($\varepsilon_r > 1$). To the best of our knowledge, the work reported here is the first RT single NP QCSE measurement on the air−glass interface. The difficulties that have hindered such measurements in the past include (i) relatively small wavelength shifts; (ii) short exciton lifetime (rapid ionization) at RT; (iii) spectral broadening due to surface charge fluctuations; (iv) requirement for large applied fields (>100 kV/cm, close to material breakdown); (v) dielectric mismatch between the semiconductor NP (large ε_r) and air ($\varepsilon_r = 1$). Due to this mismatch, most of the applied field is dropped near the electrodes and not across the particle. Nonetheless, we were able to measure QCSE of single NPs at RT for eight different samples of different compositions and geometries. Using modulation spectroscopy and averaging, we could measure the effect even for NPs with relatively small polarizability (such as sample #1 through #6). Moreover, taking geometry and material composition into account, we could qualitatively and quantitatively reproduce experimental results in simulations, including the NPs field dependence ($\Delta\lambda-F$).

We find (both experimentally and in simulations) that the strong Coulomb interaction in type-I NPs (samples #1 and #2) results in a small QCSE ($\Delta\lambda <$ 4 nm). This is the manifestation of a minute field-induced band bending that does not alter much the electron's and hole's potential energy minima (and therefore only slightly reduces the Coulomb attraction energy). The insensitivity of the effect to length (Figure S10) is also an indication for small perturbation to the Coulomb interaction in these particles. Since NPs from samples #1 and #2 display a quadratic $\Delta\lambda-F$ relation, it is possible to use the well-known energy (E)−field (F) expression $\Delta E = \alpha F^2$ to evaluate α, the polarizability of these NPs. We find $\alpha = 1.82 \times 10^5$ Å^3 for sample #1 and $\alpha = 2.20 \times 10^5$ Å^3 for sample #2. It is noted that a similar polarizability value (2.38×10^5 Å^3) was found for a 5.8 nm diameter QD in ref 28 (even though that QD sample had a different geometry).

Asymmetric quasi-type-II NRs (samples #3 and #4) display only very slightly larger QCSE (average $\Delta\lambda \approx$ 0.7 nm) as compared to type-I NPs (average $\Delta\lambda \approx$ 0.6 nm). Since the position (and symmetry) of the QD seed in the seeded rod structure is not well-controlled or defined, their $\Delta\lambda-F$ relation is somewhere between linear and quadratic.[41] They also exhibit only a weak length and orientation dependence (Figure S10). Nonetheless, a few individual NRs from these samples, most likely well-aligned with the direction of the applied field, exhibited clear zigzag pattern in the integrated intensity and peak wavelength signals (Figure 2). Simulations show that these samples have a reduced overlap integral overall (as compared to samples #1 and #2) and an additional sudden drop around 300 to 400 kV/cm, suggesting a weaker Coulomb interaction and exciton ionization at these large fields ($\Delta\lambda$, however, is smaller as compared to the value measured for similar particles at cryogenic temperatures[41]).

Symmetric type-II QDs (samples #5 and #6) exhibit the smallest averaged QCSE ($\Delta\lambda$ = 0.5 and 0.4 nm, respectively). Simulations predict even a smaller shift (Table 2). Due to their small size and symmetric shape, charge separation is very limited for these particles, as evidenced by Figure 5a: they have a larger overlap integral with respect to the larger rod-shaped samples #7 and #8 (due to their smaller size) but smaller overlap integral with respect to samples #1 and #2 since they are type-II. As expected, these spherically symmetric samples have a quadratic $\Delta\lambda-F$ relation, exhibiting only red shifts.

Asymmetric type-II NRs (samples #7 and #8) exhibit the largest spectral shifts. Charge separation is enhanced in these structures since the minimum energy for the electron is on one side of the interface, while the minimum energy for the hole is on the other side of the interface, leading to a reduced Coulomb attraction between the separated charge carriers. This, in turn, leads to a larger response to an external field. The breaking of symmetry at the interface leads to a blue shift when the field is aligned in a direction that "pushes" the electron's and hole's wave functions toward the interface (and toward each other) and a red shift when the field is in the opposite direction, that is, "pulls apart" the electron's and hole's wave functions away from the interface (Figure 4). The largest observed red shifts are $\Delta\lambda$ = 8.2 and 13.1 nm for samples #7 and #8, respectively, values which are almost 2× and 3× larger than the values for samples #1 through #6. The largest observed blue shifts were also sizable ($\Delta\lambda$ = 7.1 and 7.3 nm for samples #7 and #8, respectively). As expected, these samples exhibit nearly linear $\Delta\lambda-F$ dependence. Interestingly, simulations confirm the experimental observation that the slope in the first quadrant (red shift) is different from the slope in the third quadrant (blue shift). The difference in slopes is attributed to the two field configurations described below.

In the case where the field pulls apart the electron and the hole away from each other, longer rods will

afford a larger charge separation, a larger dipole ($\mu = q \times d$, where μ is dipole moment, q is electron charge, d is distance between e and h), a reduced Coulomb attraction, and therefore a larger $\Delta\lambda$ red shift. The red shifts obtained for samples #7 and #8 are much larger than the shifts measured for samples #1 and #2, signifying the importance of the type-II interface. However, symmetric core/shell type-II structures (sample #5 and #6) lack the geometry that affords the generation of a large dipole. In short, the largest red shifts are achieved for elongated, asymmetric, type-II heterostructures.

In the case where the field pushes the electron and the hole toward the interface (and toward each other), the geometry of the rod plays a less important role. Instead, the band tilting due to the external applied field and the redistribution of charges form triangle potential wells for both the electron and the hole. The blue shift is a measure for the degree of tilting due to the established internal electric field (which is proportional to the external field). In the above discussion, we treated rods as 1D wires; geometry could have a secondary effect on the blue shift when the true 3D structure of the NR is taken into account. It is noted that the blue shift configuration is advantageous for cases where the size of the sensor matters, but that the red shift configuration affords the highest voltage sensitivity.

Three distinct classes of $\Delta\lambda-F$ relations were observed: (1) symmetric NPs with strong Coulomb attraction (type-I) display a red shift with a quadratic $\Delta\lambda-F$ (and $\Delta E-F$) dependence, $\Delta E = \alpha F^2$,[28] which is characterized by the polarizability α; (2) asymmetric NRs with reduced Coulomb attraction (type-II) display a red shift with a linear $\Delta\lambda$-F (and ΔE-F) dependence at zero toward positive electric fields, $\Delta E = F \times d$ (d is distance);[30] (3) asymmetric NRs with reduced Coulomb attraction (type-II) display a blue shift with nearly linear $\Delta\lambda$-F (and ΔE-F) dependence at zero toward negative electric fields, $\Delta E = (9hq/(16(2m^*)^{1/2})^{2/3} \times F^{2/3}$, $(1/m^*) = (1/m_e^*) + (1/h_e^*)$,[47] where h is Plank's constant, q is electron charge, and m_e^* and m_h^* are effective masses of the electron and hole, respectively.

A sudden transition from a quadratic to a linear $\Delta\lambda-F$ dependence could occur at large enough fields, manifesting the ionization of the exciton, that leads to a decrease in the overlap integral and an increase in the red shift. Such critical behavior was observed for sample #4 at ~300−400 kV/cm. Samples #7 and #8, however, display such ionization already at a zero field due to their type-II nature. Exciton ionization could not be observed for type-I NRs (samples #1 and #2).

When we use these NPs for field sensing application, we need to take into account spectral diffusion. Charge trapping at the NP surface directly affects the magnitude of QCSE by changing the electric field inside the NP. If charge trapping is dynamic, it induces spectral diffusion.[48] The resulting spread of wavelengths due to such diffusion is not larger than 10 nm.[33,49] In our observation, emission peaks diffuse no more than 4 nm (Figures 1d, 2d, and 3d), consistent with the earlier works. Interestingly, our results suggest that trapped charges have a strong influence on V_{on} states (Figure 1d, 2d, and 3d, red) as compared to V_{off} states. This is likely because the wave function is more susceptible to the trapped charges when it is close to the surface of the NP. Obviously, spectral diffusion due to trapped charges reduces the signal-to-noise ratio (S/N) in voltage sensing, especially for short integration times. Generally, we observed that if the average shift is larger than 4 nm, reliable voltage sensing could be achieved despite spectral diffusion.

In summary, our observations indicate that the QCSE magnitude and applied field dependence are sensitive to the shape and the material composition of the nanoparticles: (i) Type-I NRs (homostructures with cylindrical symmetry) only weakly respond to the applied field (Figure 1). The magnitude of their QCSE shift is small, and the signal is usually masked by spectral diffusion at RT (likely due to local charge fluctuations/redistributions). With signal averaging, some weak signals could be measured above the noise. As reported earlier,[29] these NRs display a quadratic field dependence (Figure 4a, black squares). Although one might expect charge separation to be dependent on the NR length, we do not observe length dependence for type-I NRs. (ii) Quasi-type-II NRs (heterostructures with cylindrical symmetry) display slightly larger QCSE than type-I NRs (Figure 2). Also, its asymmetric composition alters its field dependence, to be no longer quadratic (Figure 4a, red diamonds). Calculations indeed confirm reduced Coulomb interaction for quasi-type-II NRs as compared to type-I NRs (Figure 5a, red diamonds *vs* black squares), allowing for larger polarizability. (iii) Type-II core/shell QDs (heterostructures with spherical symmetry) display the weakest QCSE, often totally masked by spectral diffusion (Figure S11a,b). This observation implies that symmetry breaking is important for sizable QCSE. The field dependence of these particles is quadratic (Figure 4a, blue triangles). (iv) Type-II NRs (heterostructures with cylindrical symmetry) display the largest QCSE (Figure 3) and close to linear field dependence (Figure 4a, dark cyan down triangles and pink left triangles). Calculations suggest that Coulomb interaction is reduced the most in these structures (Figure 5a, dark cyan down triangles and pink left triangles), affording large polarizability. The symmetry breaking by the type-II heterostructure is manifested through the close to linear field dependence. The large shifts in these samples are hardly affected by spectral diffusion.

CONCLUSIONS

We measured and simulated wavelength shifts for eight different NP formulations on the single molecule

level at room temperature. We found that type-II asymmetric NRs ZnSe−CdS and CdSe(Te)−CdS−CdZnSe yielded the largest shifts, demonstrating single particle sensitivity of $\Delta\lambda/\lambda \sim 2.1\%$ at a field of 400 kV/cm. The shifts for these samples (#7 and #8) were roughly linear with the applied external field and displayed both red and blue shifts within a broad range of applied voltages, depending on the field's polarity with respect to the particle's orientation. The demonstrated sensitivity could be translated into a noise-immune, ratiometric voltage measurement of two spectral bands (by splitting the fluorescence with an appropriate dichroic mirror followed up by band-pass filtering the two spectral bands using two detectors).

The temporal response of the Stark effect is in the nanosecond range. If voltage measurements are to be performed with NPs on the ensemble level, very fast signals could indeed be detected. The voltage nanosensors presented here, however, are capable of reporting voltage signals on the single particle level. For this, though, enough photons need to be detected from a single nanosensor to yield a reasonable signal-to-noise-ratio. We demonstrated here discernible shifts measured on single nanosensors with 30−100 ms time resolution. With further optimization, stronger laser excitation, faster cameras, brighter QDs, and better QDs' coating, we could expect significant improvements in single nanosensor time resolution.

We believe that the results reported here could be further enhanced by (i) improving synthesis to yield even more uniform particles; (ii) engineering electron and hole wave functions that display weaker exciton binding energy while maintaining high radiative recombination rate (by improving on band gap structure, composition, and geometry); (iii) reducing electrode spacing such that most of the field drops on the NPs; and (iv) matching the environment's dielectric constant to that of the particles or identification of asymmetric type-II structure with lower dielectric constant. With such improvements, these voltage nanosensors could possibly find interesting applications.

Conflict of Interest: The authors declare no competing financial interest.

Acknowledgment. We thank Dr. Y. Ebenstein for help with the optical setup, Dr. X. Michalet for help with measurement automation, and K. Sato and A. Pan for useful discussions of quantum calculation. This work was supported by NIH Grant Nos. 5R01EB000312 and 1R01GM086197 (to S.W.), BSF Grant No. 2010382 (to S.W. and D.O.), and ERC (to D.O., Starting Investigator Grant No. 258221 SINSLIM).

Supporting Information Available: SI-1, Colloidal synthesis; SI-2, pattern of the interdigitated electrode; SI-3, AC dielectrophoresis NR alignment; SI-4, optical setup; SI-5, data analysis; SI-6, simulations; SI-7, dimensions and parameters used in the simulations; SI-8, wavelength shift ($\Delta\lambda$) histograms; SI-9, spectrum of sample #8. This material is available free of charge *via* the Internet at http://pubs.acs.org.

REFERENCES AND NOTES

1. Peng, X.; Manna, L.; Yang, W.; Wickham, J.; Scher, E.; Kadavanich, A.; Alivisatos, A. P. Shape Control of CdSe Nanocrystals. *Nature* **2000**, *404*, 59–61.
2. Murray, C. B.; Norris, D. J.; Bawendi, M. G. Synthesis and Characterization of Nearly Monodisperse CdE (E = Sulfur, Selenium, Tellurium) Semiconductor Nanocrystallites. *J. Am. Chem. Soc.* **1993**, *115*, 8706–8715.
3. Peng, Z. A.; Peng, X. Nearly Monodisperse and Shape-Controlled CdSe Nanocrystals *via* Alternative Routes: Nucleation and Growth. *J. Am. Chem. Soc.* **2002**, *124*, 3343–3353.
4. Tang, J.; Sargent, E. H. Infrared Colloidal Quantum Dots for Photovoltaics: Fundamentals and Recent Progress. *Adv. Mater.* **2011**, *23*, 12–29.
5. Michalet, X.; Pinaud, F. F.; Bentolila, L. A.; Tsay, J. M.; Doose, S.; Li, J. J.; Sundaresan, G.; Wu, A. M.; Gambhir, S. S.; Weiss, S. Quantum Dots for Live Cells, *In Vivo* Imaging, and Diagnostics. *Science* **2005**, *307*, 538–544.
6. Xu, X.; Sun, B.; Berman, P. R.; Steel, D. G.; Bracker, A. S.; Gammon, D.; Sham, L. J. Coherent Population Trapping of an Electron Spin in a Single Negatively Charged Quantum Dot. *Nat. Phys.* **2008**, *4*, 692–695.
7. Mora-Seró, I. N.; Bisquert, J. Breakthroughs in the Development of Semiconductor-Sensitized Solar Cells. *J. Phys. Chem. Lett.* **2010**, *1*, 3046–3052.
8. Kim, T.-H.; Cho, K.-S.; Lee, E. K.; Lee, S. J.; Chae, J.; Kim, J. W.; Kim, D. H.; Kwon, J.-Y.; Amaratunga, G.; Lee, S. Y.; *et al.* Full-Colour Quantum Dot Displays Fabricated by Transfer Printing. *Nat. Photonics* **2011**, *5*, 176–182.
9. Manna, L.; Scher, E. C.; Alivisatos, A. P. Synthesis of Soluble and Processable Rod-, Arrow-, Teardrop-, and Tetrapod-Shaped CdSe Nanocrystals. *J. Am. Chem. Soc.* **2000**, *122*, 12700–12706.
10. Kim, S.; Fisher, B.; Eisler, H.-J.; Bawendi, M. Type-II Quantum Dots: CdTe/CdSe(Core/Shell) and CdSe/ZnTe(Core/Shell) Heterostructures. *J. Am. Chem. Soc.* **2003**, *125*, 11466–11467.
11. Carbone, L.; Nobile, C.; De Giorgi, M.; Sala, F. D.; Morello, G.; Pompa, P.; Hytch, M.; Snoeck, E.; Fiore, A.; Franchini, I. R.; *et al.* Synthesis and Micrometer-Scale Assembly of Colloidal CdSe/CdS Nanorods Prepared by a Seeded Growth Approach. *Nano Lett.* **2007**, *7*, 2942–2950.
12. Dorfs, D.; Salant, A.; Popov, I.; Banin, U. ZnSe Quantum Dots within CdS Nanorods: A Seeded-Growth Type-II System. *Small* **2008**, *4*, 1319–1323.
13. Oron, D.; Kazes, M.; Banin, U. Multiexcitons in Type-II Colloidal Semiconductor Quantum Dots. *Phys. Rev. B* **2007**, *75*, 035330.
14. Klimov, V. I.; Ivanov, S. A.; Nanda, J.; Achermann, M.; Bezel, I.; McGuire, J. A.; Piryatinski, A. Single-Exciton Optical Gain in Semiconductor Nanocrystals. *Nature* **2007**, *447*, 441–446.
15. Avidan, A.; Oron, D. Large Blue Shift of the Biexciton State in Tellurium Doped CdSe Colloidal Quantum Dots. *Nano Lett.* **2008**, *8*, 2384–2387.
16. Medintz, I. L.; Stewart, M. H.; Trammell, S. A.; Susumu, K.; Delehanty, J. B.; Mei, B. C.; Melinger, J. S.; Blanco-Canosa, J. B.; Dawson, P. E.; Mattoussi, H. Quantum-Dot/Dopamine Bioconjugates Function as Redox Coupled Assemblies for *In Vitro* and Intracellular pH Sensing. *Nat. Mater.* **2010**, *9*, 676–684.
17. Callan, J.; Mulrooney, R.; Kamila, S.; McCaughan, B. Anion Sensing with Luminescent Quantum Dots—A Modular Approach Based on the Photoinduced Electron Transfer (PET) Mechanism. *J. Fluoresc.* **2008**, *18*, 527–532.
18. Ruedas-Rama, M. J.; Hall, E. A. H. Azamacrocycle Activated Quantum Dot for Zinc Ion Detection. *Anal. Chem.* **2008**, *80*, 8260–8268.
19. Aouani, H.; Itzhakov, S.; Gachet, D.; Devaux, E. S.; Ebbesen, T. W.; Rigneault, H.; Oron, D.; Wenger, J. R. M. Colloidal Quantum Dots as Probes of Excitation Field Enhancement in Photonic Antennas. *ACS Nano* **2010**, *4*, 4571–4578.
20. Li, S.; Zhang, K.; Yang, J.-M.; Lin, L.; Yang, H. Single Quantum Dots as Local Temperature Markers. *Nano Lett.* **2007**, *7*, 3102–3105.

21. Choi, C. L.; Koski, K. J.; Olson, A. C. K.; Alivisatos, A. P. Luminescent Nanocrystal Stress Gauge. *Proc. Natl. Acad. Sci. U.S.A.* **2010**, *107*, 21306–21310.
22. Müller, J.; Lupton, J. M.; Rogach, A. L.; Feldmann, J.; Talapin, D. V.; Weller, H. Monitoring Surface Charge Migration in the Spectral Dynamics of Single CdSe/CdS Nanodot/Nanorod Heterostructures. *Phys. Rev. B* **2005**, *72*, 205339.
23. Miller, D. A. B.; Chemla, D. S.; Damen, T. C.; Gossard, A. C.; Wiegmann, W.; Wood, T. H.; Burrus, C. A. Band-Edge Electroabsorption in Quantum Well Structures: The Quantum-Confined Stark Effect. *Phys. Rev. Lett.* **1984**, *53*, 2173–2176.
24. Miller, D.; Chemla, D.; Damen, T.; Wood, T.; Burrus, C.; Gossard, A.; Wiegmann, W. The Quantum Well Self-Electrooptic Effect Device: Optoelectronic Bistability and Oscillation, and Self-Linearized Modulation. *IEEE J. Quantum Electron.* **1985**, *21*, 1462–1476.
25. Kuo, Y.-H.; Lee, Y. K.; Ge, Y.; Ren, S.; Roth, J. E.; Kamins, T. I.; Miller, D. A. B.; Harris, J. S. Strong Quantum-Confined Stark Effect in Germanium Quantum-Well Structures on Silicon. *Nature* **2005**, *437*, 1334–1336.
26. Yan, L. Voltage-Dependent Electroluminescence from Colloidal CdSe/ZnS Quantum Dots. *Appl. Phys. Lett.* **2007**, *91*, 243114.
27. Yakimov, A. I.; Dvurechenskii, A. V.; Nikiforov, A. I.; Ulyanov, V. V.; Milekhin, A. G.; Govorov, A. O.; Schulze, S.; Zahn, D. R. T. Stark Effect in Type-II Ge/Si Quantum Dots. *Phys. Rev. B* **2003**, *67*, 125318.
28. Empedocles, S. A.; Bawendi, M. G. Quantum-Confined Stark Effect in Single CdSe Nanocrystallite Quantum Dots. *Science* **1997**, *278*, 2114–2117.
29. Rothenberg, E.; Kazes, M.; Shaviv, E.; Banin, U. Electric Field Induced Switching of the Fluorescence of Single Semiconductor Quantum Rods. *Nano Lett.* **2005**, *5*, 1581–1586.
30. Hewa-Kasakarage, N. N.; Kirsanova, M.; Nemchinov, A.; Schmall, N.; El-Khoury, P. Z.; Tarnovsky, A. N.; Zamkov, M. Radiative Recombination of Spatially Extended Excitons in (ZnSe/CdS)/CdS Heterostructured Nanorods. *J. Am. Chem. Soc.* **2009**, *131*, 1328–1334.
31. Matiukas, A.; Mitrea, B. G.; Qin, M.; Pertsov, A. M.; Shvedko, A. G.; Warren, M. D.; Zaitsev, A. V.; Wuskell, J. P.; Wei, M.-d.; Watras, J.; *et al.* Near-Infrared Voltage-Sensitive Fluorescent Dyes Optimized for Optical Mapping in Blood-Perfused Myocardium. *Heart Rhythm* **2007**, *4*, 1441–1451.
32. Deutsch, Z.; Schwartz, O.; Tenne, R.; Popovitz-Biro, R.; Oron, D. Two-Color Antibunching from Band-Gap Engineered Colloidal Semiconductor Nanocrystals. *Nano Lett.* **2012**, *12*, 2948–2952.
33. Dias, E. A.; Grimes, A. F.; English, D. S.; Kambhampati, P. Single Dot Spectroscopy of Two-Color Quantum Dot/Quantum Shell Nanostructures. *J. Phys. Chem. C* **2008**, *112*, 14229–14232.
34. Miller, D. A. B. Optical Bistability in Self-Electro-optic Effect Devices with Asymmetric Quantum Wells. *Appl. Phys. Lett.* **1989**, *54*, 202–204.
35. Haywood, S. K.; Lim, A. C. H.; Gupta, R.; Emery, S.; Hogg, J. H. C.; Hewer, V.; Stavrinou, P. N.; Hopkinson, M.; Hill, G. Demonstration of a Blueshift in Type II Asymmetric InP/InAsP/InGaAs Multiple Quantum Wells. *J. Appl. Phys.* **2003**, *94*, 3222–3228.
36. Nirmal, M.; Dabbousi, B. O.; Bawendi, M. G.; Macklin, J. J.; Trautman, J. K.; Harris, T. D.; Brus, L. E. Fluorescence Intermittency in Single Cadmium Selenide Nanocrystals. *Nature* **1996**, *383*, 802–804.
37. Pelton, M. Characterizing Quantum-Dot Blinking Using Noise Power Spectra. *Appl. Phys. Lett.* **2004**, *85*, 819.
38. Frantsuzov, P.; Kuno, M.; Janko, B.; Marcus, R. A. Universal Emission Intermittency in Quantum Dots, Nanorods and Nanowires. *Nat. Phys.* **2008**, *4*, 519–522.
39. Kuno, M. Nonexponential Blinking Kinetics of Single CdSe Quantum Dots: A Universal Power Law Behavior. *J. Chem. Phys.* **2000**, *112*, 3117.
40. Talapin, D. V.; Koeppe, R.; Götzinger, S.; Kornowski, A.; Lupton, J. M.; Rogach, A. L.; Benson, O.; Feldmann, J.; Weller, H. Highly Emissive Colloidal CdSe/CdS Heterostructures of Mixed Dimensionality. *Nano Lett.* **2003**, *3*, 1677–1681.
41. Müller, J.; Lupton, J. M.; Lagoudakis, P. G.; Schindler, F.; Koeppe, R.; Rogach, A. L.; Feldmann, J.; Talapin, D. V.; Weller, H. Wave Function Engineering in Elongated Semiconductor Nanocrystals with Heterogeneous Carrier Confinement. *Nano Lett.* **2005**, *5*, 2044–2049.
42. Kraus, R. M.; Lagoudakis, P. G.; Rogach, A. L.; Talapin, D. V.; Weller, H.; Lupton, J. M.; Feldmann, J. Room-Temperature Exciton Storage in Elongated Semiconductor Nanocrystals. *Phys. Rev. Lett.* **2007**, *98*, 017401.
43. Sitt, A.; Sala, F. D.; Menagen, G.; Banin, U. Multiexciton Engineering in Seeded Core/Shell Nanorods: Transfer from Type-I to Quasi-Type-II Regimes. *Nano Lett.* **2009**, *9*, 3470–3476.
44. Haas, H.; Magnea, N.; Dang, L. S. Quantum-Confined Stark Effect on Spatially Indirect Excitons in CdTe/Cd_xZn_{1-x} Te Quantum Wells. *Phys. Rev. B* **1997**, *55*, 1563–1567.
45. Wang, S.; Wang, L.-W. Exciton Dissociation in CdSe/CdTe Heterostructure Nanorods. *J. Phys. Chem. Lett.* **2010**, *2*, 1–6.
46. Susa, N. Quantum-Confined Stark Effects in Semiconductor Quantum Disks. *IEEE J. Quantum Electron.* **1996**, *32*, 1760–1766.
47. Aspnes, D. E. Electric-Field Effects on Optical Absorption near Thresholds in Solids. *Phys. Rev.* **1966**, *147*, 554–566.
48. Empedocles, S. A.; Bawendi, M. G. Influence of Spectral Diffusion on the Line Shapes of Single CdSe Nanocrystallite Quantum Dots. *J. Phys. Chem. B* **1999**, *103*, 1826–1830.
49. Blanton, S. A.; Hines, M. A.; Guyot-Sionnest, P. Photoluminescence Wandering in Single CdSe Nanocrystals. *Appl. Phys. Lett.* **1996**, *69*, 3905–3907.